Does speed kill or make friction better?—Designing materials for high velocity sliding

S.J. Eder [a,b,*], P.G. Grützmacher [b], M. Rodríguez Ripoll [a], C. Gachot [b], D. Dini [c]

[a] AC2T research GmbH, Viktor-Kaplan-Straße 2/C, Wiener Neustadt 2700, Austria
[b] Institute for Engineering Design and Product Development, TU Wien, Lehárgasse 6 – Objekt 7, Vienna 1060, Austria
[c] Department of Mechanical Engineering, Imperial College London, South Kensington Campus, Exhibition Road, London SW7 2AZ, UK

A R T I C L E   I N F O

A B S T R A C T

Many modern applications rely on the safe operation of components sliding at high speeds, e.g., in the fields of e-mobility, high-speed manufacturing, or impact-resistant materials. While the impact of mechanical energy and heat on the friction and wear behavior of dry metallic interfaces has been the focus of extensive research in the past, the effect of extreme speeds on the near-surface deformation mechanisms in polycrystalline metals has remained poorly understood. In this work, we have tackled this crucial issue by exploring sliding velocities ranging from 10 to 2560 m/s via large-scale molecular dynamics simulations to identify three distinct deformation regimes in CuNi alloys. The microstructural response does not vary much for any of the considered systems up to sliding velocities of 40 m/s, but then evolves drastically up to a maximum value located between 320 and 1280 m/s depending on the composition. We observe that the degree of plastic deformation at the highest sliding speeds drops down to a level almost as low as for the lowest sliding speeds. We attribute this behavior to a sharp increase in the contact temperature at these high sliding speeds, approaching or even exceeding the bulk melting temperature, which goes hand in hand with a decline in the contact area and the resistance to sliding. Our characterization of the non-linear and non-monotonic material response to increasing sliding velocities will aid the systematic selection of materials and the design of robust components for a variety of high-speed sliding and wear applications.

1. Introduction

Speed, as a quantity influencing the kinetic energy of a system, has substantial effect on many processes. This ranges from charging speed dependent battery life [1], over crystallization processes [2] to material plasticity [3,4]. Sliding velocity also affects friction and, more in general, the behavior of contacting interfaces, where the interactions between surfaces are extremely complex and affected by material pairing, applied loads, the environment, presence of lubricants and surface contamination, as well as by the evolution of the topography and the microstructure, to name some of the most important influences [5]. Yet, the third of the three fundamental laws of friction by Coulomb states that kinetic friction is independent of the velocity [6]. Despite this being true for many cases on the macroscopic scale, deviations from this law are observed, particularly for high speeds. There are several factors contributing to these deviations. Many metals exhibit increasing strength with higher strain rates, resulting in a lower real area of contact

and hence, friction [7]. On the other side, high sliding speeds may lead to high interface temperatures in the frictional contact, thus reducing the shear strength of the material or even inducing localized melting [7]. In the case of melt formation, friction depends on viscous forces in the liquid layer, which results in a smaller resistance to sliding and lower friction [8]. The phenomenon of localized melting for high velocities resulting in coefficients of friction (CoF) as low as 0.02 was already reported by Lim and Ashby, who derived wear and friction-regime maps for dry sliding of steel surfaces [9,10]. Later, Molinari et al. investigated the impact of velocity on the CoF theoretically and added another failure mechanism of the adhesive junctions by adiabatic shear banding [8]. Furthermore, they demonstrated a significant decrease in friction for steel-on-steel contacts close to the sliding velocity where melting occurs. Another factor contributing to lower friction at high velocities is the formation of lubricating oxides at higher temperatures [11]. Even though not universal, the general trend is that friction decreases with increasing speed. Such considerations are of interest for applications and

processes where high speeds and high shear rates prevail, including brakes, clutches, crash performance of automotive components [12], high-speed metal fabrication [13], turbine engines [14], explosive welding [15], gun barrels [16], but recently also in the field of electromobility for high-speed electrical motors [17]. Despite all these processes being grouped under the term "high-speed dynamics", typical sliding velocities cover several orders of magnitude with different deformation mechanisms being dominant [18,19]. The performance of automotive components during crash is found at the lowest range (10 to 20 m/s) and is characterized by the dominance of strain rate dependent plasticity. Under these conditions, viscous drag forces acting on dislocations become dominant in comparison to strain-rate-independent plasticity, where hardening is dominated by dislocation forest interactions or by the interaction between dislocations, grain boundaries, and precipitates [19,20]. Relative sliding velocities in the range of 50 to 150 m/s are characteristic of machining processes such as grinding [21, 22], but also apply to the next generation of ball bearings and transmissions for electrical motors, where manufacturers are heading towards rotational speeds of 30,000 rpm with grease-lubricated ball bearings [23], with the increased heat generation rate causing significant strain to the bearing materials [24]. At the other extreme, supersonic projectiles [16], permanent magnet drives for turbochargers [25], and processes associated with technologies such as explosive welding [15,26] result in interface velocities of 1000 m/s and beyond. These velocities and the associated high shear rates are often accompanied by significant frictional heating, leading to a decrease in the resistance to shear induced by surface melting [27]. The access to experimental data for materials sliding at extreme velocities requires the use of specialized laboratory equipment. Examples of devices able to perform friction experiments under extreme shear rates include modified Hopkinson bars covering the range up to 60 m/s, milling devices with a similar velocity range, and frictional welding equipment, with maximum velocities limited to a few m/s. The access to experimental friction data for velocities beyond 100 m/s is non-trivial, and results are scarce in the available literature [16,28].

In contrast to mesoscale or macroscale observations [29], friction at the atomic scale between a tip of a friction force microscope (FFM) and NaCl was shown to increase with sliding speed at extremely low sliding speeds (nm/s –μm/s) [30]. In the FFM, a single asperity contact is modeled, where thermal activation of the irreversible jumps of the tip leads to hysteretic behavior of lateral forces and to the observed speed dependence. Looking at friction alone gives a limited view on the effect of sliding speed, as the observed friction forces are a result of various energy dissipating processes occurring in the sliding zone near the surface. The major part of the energy is dissipated in the form of heat, leading to the aforementioned increase in interface temperature, but a portion of the remaining energy is used to plastically deform the material and create new surface area and defects in the material [8,11]. Both plastic deformation and heat generation can have a pronounced effect on the microstructutral evolution in the near-surface zone [31–33]. Changes in the microstructure in these near-surface zones in turn affect the mechanical properties and, in consequence, also the tribological properties [34,35]. Adding a material science perspective into the investigation of friction and wear is crucial for optimizing these properties, thus facilitating the design of more efficient, long-lasting, and sustainable engineering parts [36].

Performing experimental studies at the length and time scales required to shed light on the microstructural mechanisms at play is a non-trivial and costly enterprise. Moreover, while some in-situ studies that show the development of polycrystalline systems under tribological loading have been undertaken [37], scientists usually have to make do with ex-post analyses of run samples. Thus, suitable computer simulations can provide an ideal complementary approach to visualizing complex phenomena and identifying the associated mechanisms. Molecular dynamics (MD) simulations, paired with modern high-performance computing facilities, can nowadays handle systems with tens to hundreds of millions of atoms for reasonable time periods (some tens of nanoseconds) [38], allowing an analysis of microstructural processes at the atomic level [31,39]. This leads to more and more possibilities to directly compare MD results with real experimental data [13,40]. MD can provide an ideal vehicle for the description of plastic deformations and to study how dislocations, twins, and grain boundaries behave collectively. However, one should bear in mind that attention must be paid when plastic flow is dominated by large dislocation speeds, especially when they approach relativistic velocities, where an unequivocal picture of the phenomenology of interacting dislocations and their dynamics has not emerged from the multitude of MD studies that have been undertaken [18]. Given that phonon drag and radiative damping are believed to dominate at such high speeds and that both phenomena are agreeable to study using discrete lattice dynamics models, it seems possible to provide general qualitative insights into the dislocation-lattice interaction, which has so far eluded the more physically rich MD simulations that these models could complement [41].

While the continuing advances that are made possible by ever-increasing computational power have led to substantial growth of the systems that can be treated using MD simulations, a considerable variation of relative speed has proven elusive. This is an intrinsic issue of MD: larger systems can in principle always be treated by increasing computational resources and evenly distributing the work load among the processor cores, but longer simulation periods require more real computation time and will invariably lead to a build-up of numerical inaccuracies. In this work, we consider copper-nickel (CuNi) systems that consist of approximately 25 million atoms for periods up to 28 ns. This allows us to reach sliding speeds as low as 10 m/s so we can study the effect of velocity on friction and near-surface material properties over a sliding speed range covering three orders of magnitude. CuNi is an ideal alloy system in which both constituents form an isomorphous system without phase precipitation, i.e., it features a "benign" phase diagram that lends itself to numerical studies. CuNi alloys have numerous applications such as in power plants, offshore oil production, and shipbuilding [42], electrical sliding contacts [43], projectile jackets, cylinder locks, brake lines, as well as in tribological interfaces of jet engine compressors [14]. Specifically important in times of the increasing electrification of our mobility is the development of reliable copper alloys for high-speed components such as bearings in electrical motors and transmission systems [24]. In these components, increasing the rotational speed can reduce the torque while keeping the electrical power output constant, thus allowing higher power densities in the electric motor and reducing the demand for rare-earth metals.

After identifying specific configurations of interest for the alloy system under investigation, based on our extensive study of the parameter space affecting its performance [33,39], in the following we present a systematic study of the effect that sliding speed has on deformation mechanisms. There exist earlier studies by other groups that have observed phenomena similar to those discussed in this work [28,44,45], but to the best of our knowledge, no single study has yet attempted to understand the occurring mechanisms at the level of detail and sophistication adopted here. Thus, this work provides new fundamental insight into the key features that govern friction in fcc metals at high velocity. The emergence of a clear picture that demonstrates the synergistic link between dislocation and twinning activity, contact temperature and area evolution as a function of speed is discussed, in what we believe is the first full mechanistic assessment of the link between microstructural evolution, thermal gradient effects, plastic flow, phase transformations, and resistance to shear. While these aspects are all closely intertwined, the mapping produced in this work can be used to control the behavior of this and a number of other similar alloys subjected to manufacturing processes, or applications that require surfaces interacting at considerable sliding speeds.

Table 1

Considered alloys (named according to their atomic Ni content), Ni content by weight, intrinsic stacking fault energy γ_{isf} (from Ref. [53]), applied normal pressure, and the sliding speed ranges applied in our simulations. The total computational expenditure exceeded 4 million CPU-h.

alloy	CuNi5	CuNi25	CuNi60	Ni
wt.% Ni	5	24	58	100
γ_{isf} (mJ/m^2)	54	79	106	153
σ_z (GPa)	0.5	0.7	1.5	3.1
v_x (m/s)	20–640	10–1 280	40–2 560	80–2 560

2. Simulation and visualization details

The compositions, normal pressures, and the temperature of the systems analyzed in this work were carefully selected based on the large amount of data available from two previous studies that were conducted at a constant sliding velocity of 80 m/s [33,39]. The goal was to select systems with distinct stacking fault energies (ranging from 54 to 153 mJ/m^2) that featured a wide range of microstructural mechanisms over time at 80 m/s, so that the sliding velocity variation would have a significant effect and could be studied in isolation. This allows us to study the increase of twinning activity, the fraction of grain boundaries and defects, the shear strain rate in the near-surface region and the bulk of the sample, the real contact area, the contact temperature, and the resistance to shear as a function of the sliding velocity for four representative alloy systems.

Our simulations were performed using the open-source MD code LAMMPS [46], which has become the de-facto standard for meshless simulations in academic tribological research. The polycrystalline model of the CuNi alloy system measures $85 \times 85 \times 40$ nm^3, contains approximately 25 million atoms, and was prepared as explained in Eder et al. [47], 48], see Fig. 1 for an overview. All CuNi alloy systems were produced from a pure Cu system via random substitution of Cu atoms with Ni atoms according to the desired Ni content. The systems were initially prepared by heat treatment and cooling to 300 K as described in Eder et al. [39]. As the lattice constant of Ni is approximately 2.5% smaller than that of Cu, but we wanted to keep the lateral system dimensions and the total number of atoms constant, the final extent of the system in z-direction slightly decreases with Ni content after the heat treatment. This leads to the pure Ni system to be some 3 nm thinner than the CuNi5 system, which must be kept in mind when calculating averages over equivalent portions of the sample microstructure. Boundary constraints were applied to the lower 3 Å of the model, where a "sacrificial layer" of$\sim$ 10 nm grains was attached to the "working layer" of$\sim$ 40 nm grains so none of the occurring mechanisms would be externally constrained. Interactions within the CuNi samples are governed by an embedded atom potential from [49].

The counterbody is a bcc Fe(100) monocrystal with a Gaussian root-mean square surface roughness of 0.5 nm, a fractal dimension of 2.186, and a characteristic lateral asperity extent of 33 nm, which are values similar to what has previously been used in literature [51], ensuring reasonable steepness of the asperity slopes. The counterbody thickness was reduced to several monolayers and kept rigid to have most of the computational resources available for the simulation of the microstructural evolution of the polycrystalline CuNi samples. This implies that the counterbody is much harder than the sample. Lennard-Jones potentials controlled the interactions between the counterbody and the sample, with the global energy parameterε = 0.095 eV obtained as described in Eder et al. [52], whileσ_{Fe-Cu} = 0.224 nm andσ_{Fe-Ni} = 0.221 nm were calculated from interatomic first-neighbor distances using the Lorentz–Berthelot mixing rules. This effectively mimics the existence of an atmosphere and avoids artifacts of stiction and cold-welding that would otherwise occur between nascent metal surfaces in ultra-high vacuum conditions.

The counterbody was moved across the surface of the sample at a

sliding velocityv_x and a small orthogonal component of$v_y = v_x \cdot 9/80$ m/s to prevent roughness features from coming into repeated contact with their own sliding marks. Thus, the sliding distances_{slide} (featured as an abscissa quantity in several of the following graphs) can be considered a perfectly controllable input parameter. The value ranges forv_x are listed in Table 1, with neighboring values differing by a factor of 2. During the simulation runs, carried out at a time step of 2 fs, the normal pressureσ_z on the sample was kept constant during sliding up to a total sliding distance of 280 nm. Theσ_z value for a particular alloy, listed in Table 1, was chosen so that all compositions undergo similar microstructural changes. Allσ_z values lie centered in the blue region of the deformation mechanism map for 300 K and 80 m/s introduced in Ref. [39] (see Fig. 1), which is associated with stress-induced grain growth and the formation of a shear layer, and should therefore feature a range of deformation mechanisms without leading to catastrophic failure. All simulations in this work may therefore be considered to be carried out along the "iso-deformation curve" shown on the right side of Fig. 1.

A Langevin thermostat with a time constant of 0.5 ps acted on all the non-rigid sample atoms to drain away the frictional heat. This implies that the phonons in the system are coupled to the electrons, which act as a heat bath to mimic the electronic contribution to the thermal conductivity in a metal [54]. The thermostat acts only perpendicular to the directions of sliding and normal pressure in order not to interfere with these external constraints.

The computational tomographs of the polycrystalline CuNi sample shown and discussed throughout this work are colored according to grain orientations as in electron backscatter diffraction (EBSD), using the inverse pole figure (IPF) coloring standard (see Ref. [55] for an in-depth discussion). Orientations were calculated using polyhedral template matching [56] as implemented in OVITO [57], and the EBSD-IPF style colors were produced using the MTEX toolbox [58,59] for Matlab.

Grain refinement/growth and twinning were quantified for each time step via common neighbor analysis (CNA) [60] with a neighborhood cutoff radius of 0.3086 nm for the CuNi alloys and 0.3005 nm for Ni. CNA itself cannot distinguish between grain boundaries, defects, and surfaces on one hand, as well as between twin boundaries, stacking faults, and Shockley partials on the other. For the sake of brevity, here we refer only to grain boundary (GB) and twin boundary (TB) atom fractions, respectively, which are the number of GB or TB atoms divided by the total number of atoms in the system.

The microstructure evolution in a given alloy for a constant contact pressure shows that the formation of a shear layer is highly dependent on the applied sliding velocity. The analysis of the shear layer in our earlier work could be restricted to its identification via some reasonable criteria and the monitoring of the evolution of its thickness [39], as the sliding velocity was fixed at a relatively low value of 80 m/s. As the sliding speeds considered now span more than three orders of magnitude, the mere definition of a shear layer via an atomic advection velocity threshold no longer seems sufficient, and the quality of the velocity depth profiles require more in-depth attention. As detailed further in Ref. [61], the atomic advection velocities were obtained by calculating the distance between the positions of an atom at two time steps that are 500–80 k time steps apart (depending on the sliding speed) and associating the obtained average velocity with the atomic position exactly between these two time steps. In this fashion, thermal fluctuations are automatically eliminated, equivalent to applying a low-pass filter. Depth- and sliding-distance-resolved maps of the atomic advection velocities were produced by space-averaging over lateral layers with a thickness of 1 nm (corresponding to approximately6×10^5 atoms). By calculating the derivatives of these velocity maps along the z direction, the shear strain rate can be obtained as a function of depth and sliding distance, which is best displayed on a logarithmic scale.

An estimate of the real contact area between the CuNi base body and the rigid Fe counterbody was calculated at each time step, based on the mathematical foundation laid out in Eder et al. [62]. Briefly

summarized, base body atoms in first-neighbor contact with atoms of the counterbody are determined based on the corresponding radial distribution function. The x and y coordinates of the base body atoms in contact were then binned in a nearly atomically resolved 2D-histogram. The number of bins with non-zero values divided by the total number of bins yield a good estimate of the relative real projected contact area (with a non-dimensional value between 0 and 1). For sanity-check purposes, the obtained values were compared with a 3D estimate of the relative real contact area, which is determined by multiplying the number of contact atoms with a per-atom contact area and dividing it by the constant lateral cross-section of the system. This 3D relative contact area may become greater than 1 if the contact is nearly fully conformal due to the roughness of the counterbody. However, the differences between the 2D and the 3D versions of the relative real contact area are slight, and the trends are identical.

The mechanical reaction forces in sliding and normal direction, F_s and F_n, respectively, were measured between the bulk of the CuNi samples and the rigid lower layer of atoms, and block-averaged to yield the same output frequency as the geometrical data. The resulting sliding-distance dependent curves were then averaged over the final 80 nm of sliding, also calculating the standard deviation in that interval. Divided by the lateral cross-section A_n of the system, this yields the shear stress $\sigma_x = F_s/A_n$.

Finally, the space-resolved temperature distribution was calculated for every geometrical snapshot. To obtain a reasonable trade-off between spatial resolution and accuracy, the domain was divided into $40 \times 20 \times 21$ cuboid elements from which the respective spatially-averaged center-of-mass velocity field was subtracted before calculating the temperature from the kinetic energy of the atoms in that element. Temperature values were output as averages over 20 consecutive time steps, and elements with less than 50 contributing atoms were discarded from the evaluation. We define the surface temperature distribution as that encompassing the 2 nm layer nearest to the base body surface, which includes 800 elements. The temperature values in this surface layer can be evaluated in terms of a top-view thermal map to study the lateral distribution of the peak temperatures, as well as in terms of histograms representing the temperature distribution for each time step, which can be arranged in a sliding-distance-resolved map. At high sliding speeds, the histograms become bimodal temperature distributions, with a clear distinction between a sharp low-temperature peak representing the non-contact regions, and a broad high-temperature peak for the contact regions. For the analysis of the surface temperature, only the latter of these peaks is evaluated to produce a mean surface temperature and its standard deviation.

3. Results and discussion

Fig. 2 shows the microstructure of a representative slice of the alloys CuNi25 at 0.7 GPa contact pressure and all investigated sliding velocities plotted at regular sliding distance intervals. Note that CuNi25 was chosen because it offers the widest range of different sliding velocity data, but the other three compositions behave correspondingly. The images clearly reveal that the sliding velocity has a pronounced effect on the microstrucutral evolution of the alloy over the observed sliding distance. For sliding velocities up to 80 m/s the microstructure remains largely unaffected during sliding with the initial grain boundaries mostly intact. For these velocity range, signs of mild plastic deformation appear for large sliding distance towards the end of the simulation, mainly as partial lattice rotation of the upper grains leading to grain refinement as well as the formation of some stacking faults, twins, and defects. Starting at 80 m/s, the grains are elongated in the direction of sliding, indicating the incipient formation of a shear layer, which we will discuss in the next paragraph. Interestingly, a further increase of the sliding velocity results in reduced microstructural changes. Paradoxically, the resulting microstructures at the end of the sliding process are extraordinarily similar for the lowest 10 m/s and the highest sliding

velocity of 1280 m/s.

Let us now analyze the shear strain rate as a function of sliding speed, sample depth, and sliding distance with the help of Fig. 3 with the composition CuNi25 serving as a representative example of behavior that occurs correspondingly for the other compositions. In panel (a) we compare normalized and time-averaged equilibrium velocity depth profiles for the entire range of sliding speeds. In this context, velocity depth profile denotes that the atomic advection velocities in sliding direction have been averaged over the lateral system dimensions, making them a function of sample depth. The aspect of time-averaged equilibrium denotes the fact that these profiles were also time-averaged over the last 80 nm of sliding, thus in most cases being near their equilibrium values. Finally, to be able to compare the profiles in a meaningful way, each profile was normalized by its corresponding sliding speed, so that the maximum atomic advection velocity is 1.

The shape of these profiles reveals a great deal about the quality of the shear layer. A Gamma (Γ) shaped profile, typical of low sliding speeds, means that all shear is strongly localized near the surface, leading to shear strain rates from 10^9 to 10^{10} within a surface layer of only 1–2 nm thick. At the same time, the mean shear strain rate in the "bulk" of the sample can be as low as approximately 10^6, which at our system size is the detection threshold for this quantity. As the sliding speed increases, the shape of the profile assumes a "shoulder" shape, see for instance the purple curve for 80 m/s in Fig. 3a, so this marks the point where sliding starts affecting the shear strain rate within the bulk of the sample. Shear is no longer localized to the near-surface layer, but rather extends throughout the entire system depth, with the shear strain rate being a function of the sample depth. As the sliding speed increases further (320 m/s), the complete aggregate experiences a high shear strain rate already after 75 nm sliding distance, which means that the entire material is being sheared and the velocity profile assumes a nearly linear form throughout the entire sample, with only a small kink at $v_x/v_{slide} \approx 0.7$. This sort of velocity profile is strongly reminiscent of Couette flow and therefore resembles the flow of a viscous fluid. The development of the shear strain rate is further visualized in panels (b) to (d), which show heat maps of the shear strain rate as a function of sliding distance and sample depth. Panel (b) visualizes the shear strain rate of the CuNi25 alloy at a sliding speed of 80 m/s, showing that the shear strain rate is initially high on the outermost layer of the material. In accordance with the 'shoulder" shape observed in panel (a), the value of the shear strain rate starts rising well in the bulk with increasing sliding time, affecting most of the aggregate by the end of the sliding time. The heat map in panel (c) reveals that the shear strain rate at 320 m/s seems to be nearly time- and depth-independent for sliding distances greater than 150 nm, while the microstructural development in row 6 of Fig. 2 is well in line with the above observations, showing a strongly sheared grain structure. At this sliding velocity, the influence of sliding speed has a maximum impact on microstructure.

A further increase of the sliding speed does not lead to a saturation of the Couette flow behavior discussed above. Conversely, the normalized velocity profile at 640 m/s assumes a shape that is almost identical to that at 80 m/s, and the corresponding heat map in panel (d) reveals that the shear strain rate is again a function of sliding distance and sample depth. At the highest considered sliding speed of 1280 m/s, the velocity profile re-assumes the Γ shape, being virtually indistinguishable from the profiles obtained at the lowest sliding speeds.

To demonstrate the flow behavior of the material, in panel (e) we normalized the average bulk shear strain rate by the ideal Couette flow. As the shear strain rate reaches higher values in increasing material depths as a function of sliding distance and sliding velocity, the motion of the material is similar to an ideal Couette flow, demonstrated by values close to 1 for a sliding velocity of 320 m/s. Again, for sliding velocities higher than this the flow behavior increasingly deviates from an ideal Couette flow as the shear layer is confined in the outermost region of the material with a decreasing bulk contribution to shear.

The frictional behavior of metal surfaces might be affected by a rise in contact temperature or a reduction of the real contact area with higher sliding speed [7], as discussed in the introduction. Therefore, the sliding speed dependent behavior of the shear strain rate discussed above might be explained by an analysis of the real contact area and the contact temperature. Based on Fig. 4, we can verify great changes in both contact temperature and real contact area, which can be observed when changing the sliding speed. Note that compositions and sliding speeds were chosen to best reflect this behavior, while the general trend is universal for all compositions, as will be demonstrated later on. For lower sliding velocities the influence of sliding speed on microstructure evolution is small and a shear layer is not well established (CuNi5@20 m/s). As the sliding velocity increases, the influence of sliding velocity on the microstructure becomes maximum (Ni@1280 m/s), which is characterized by an increase in the contact area, severe plastic deformation, with the microstructure evolving as a shear layer with a Couette flow and a rise in surface temperature. For the largest sliding velocities, a significant rise in surface temperature is observed, coincident with a drastic reduction in contact area and a very low degree of plastic deformation (CuNi60@2560 m/s). In Fig. S2 in the Supplementary Material, we plot the time-development of the relative real contact area $A_c^{(rel)}$ to ascertain that the end values well represent the equilibrium values. From this graph, we read that typical values for $A_c^{(rel)}$ range from 10 to 80%. The top row of Fig. 4 shows top-views of the sample surface with only those atoms contributing to the contact area being colored according to their topographic value, i.e., the lowest-lying atoms are blue and the highest-lying ones red. This implies that approximate contact pressures would be exactly reversed, i.e., high pressures in blue and low ones in red. While the left column (CuNi5@20 m/s) represents a lightly loaded tribosystem with approximately 20% of surface atoms being in contact, the central column (Ni@1280 m/s) exhibits almost full contact conformity as a result of high plastic deformation during sliding. What is perhaps most surprising though is that CuNi60@2560 m/s in the right column only has just over 10% of its surface atoms in contact with the counterbody, which according to the graph in Fig. S2 also seems to be a very stable value. It can thus be stated that here the sliding speed has a dominating influence on the contact area between substrate and counterbody, and will therefore have a pronounced effect on the resulting friction behavior.

The second row of panels in Fig. 4 shows the surface temperature distribution of the snapshots directly above. For lower sliding velocities (CuNi5@20 m/s), there seems to be no discernible influence of the contact spot structure on the temperature distribution, and the typical contact temperature lies only 5–10 K above the thermostat target temperature of 300 K. The negligible development of frictional heat despite the small contact area and the accompanying high contact pressures is a result of fast removal of heat by the thermostat. This changes noticeably when the influence of the sliding speed is at its maximum, see the central column. There now emerge loosely bounded regions of elevated contact temperature up to 900 K, which closely correlate with the regions in the contact area plot above that mark where the rigid counterbody indents deepest into the Ni sample (shown in blue). The areas lying outside the high-pressure contact regions remain relatively cool at around 400 K. Finally, at very high sliding speeds, the contact area drops dramatically, as mentioned above, leading to distinct "islands" with temperatures going up to 3500 K, while the regions between these contact spots remain at a relatively homogeneous 500 K. The fact that 3500 K lies well above the melting temperature of Ni (1752 K), while the non-contact regions lie comfortably below, suggest that the contact spots are actually in a liquid state, possibly acting as a lubricant, and that there must be phase transitions occurring repeatedly between those areas that are in contact and those that are not.

To shed light on this, in the bottom row of Fig. 4 we also show microstructural cross-sections of the systems, taken at the position marked by the dashed white line and colored according to grain

orientation, as the images shown in Fig. 2. Among the more relevant features are the gaps between the sample and the gray counterbody, which are clearly visible for CuNi5@20 m/s (left) and CuNi60@2560 m/s (right), but not for Ni@1280 m/s in the center because of the almost full contact conformity. It is also clear that Ni@1280 m/s has undergone drastic microstructural changes and exhibits evidence of stress-assisted grain growth that has taken place alongside the formation of a shear layer. By comparison, the counterparts to the left and the right show much less evidence of plastic deformation, with some stacking faults, twinning, and sub-grain formation visible. Additional details about the contact zone between substrate and counterbody are visualized in magnifications of the respective contact zones of the three systems. It can be seen as evidence for the assumption that phase transitions occur between the contact and non-contact regions in the case of the CuNi60 system at 2560 m/s, that directly below the contacting asperities of the counterbody, there are regions of a thickness of approximately 2.5 nm that appear to be so noisy that they must be considered amorphous or liquid, while the near-surface regions in the non-contact areas are defect-rich, but definitely crystalline. Figure S4 in the Supplementary Material shows the radial distribution functions of near surface regions for the system CuNi60 at 2560 m/s before (blue), during (red) and after (green) asperity contact. Before the asperity contact, the radial distribution function, describing how density varies as a function of radial distance from a reference particle, clearly denotes distinct and repetitive peaks in the spectrum typically found for crystalline solids. During the asperity contact, highlighted in red, the radial distribution function does not show anymore sharp and repetitive peaks apart from the first peak indicating the first coordination sphere of a liquid or an amorphous system. After the asperity contact (green curve), peaks reappear in the radial distribution function, which are likely to be linked to recrystallization taking place. The systems representing the other two deformation modes do also appear more noisy at the contact spots but to a far lesser extent. A slow-motion movie in the Supplementary Material illustrates the repeated recrystallization processes originating at the trailing edges of the contact zones. We therefore assume that the energy requirements for the repeated phase transitions are high enough to prevent the regions below the near-surface zone to strongly deform.

Fig. 5 summarizes the sliding velocity dependence of several space- and time-averaged key quantities: the twin boundary and stacking fault fraction ΔTB (panel a), the grain boundary and defect fraction ΔGB (b), the shear strain rate (c), the relative real contact area (d), the mean contact temperature (e), and the mean shear stress (f). The respective error bars originate from the variation over time during the averaging period towards the end of the simulation, typically over the last 80 nm of sliding. Before we discuss the relevance of the velocity trends, we would like to remind the reader that all these data were collected along an "iso-high-deformation curve" at a sliding velocity of 80 m/s, extracted from the deformation mechanism map discussed in Ref. [39]. This curve lies in the region, where the microstructural evolution during sliding is dominated by stress-induced grain growth.

We observe a negligible or small increase of the key quantities with sliding speed for the lowest considered sliding speeds. In all panels except (e), starting from a specific composition dependent sliding velocity, the quantities start growing at a faster rate, culminating in a maximum value that also depends on the composition, with a subsequent drop to values similar to those associated with much lower sliding speeds.

Consistent with the location and order of the boundaries in the deformation mechanisms map, we observe that also as a function of speed, the order of the occurrence of effects is a rise in twin boundaries (panel a), then a rise in grain boundaries being indicative of grain refinement (b), and then the formation of a shear layer (c). In accordance with the results presented in Fig. 2 there are very little microstructural changes happening for the lowest sliding speeds, with is reflected by the low fractions in twin boundaries and grain boundaries up to sliding speeds of 40 and 80 m/s for twin and grain boundaries,
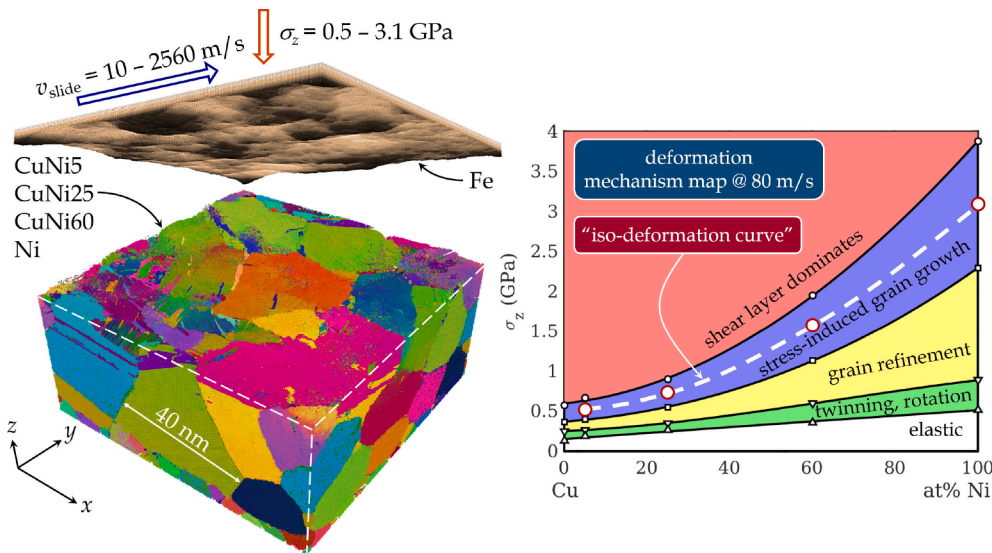
respectively (panel a and b). At 40 m/s more twin boundaries or stacking faults appear for all compositions, whose formation is energetically less expensive compared to dislocation or grain boundary formation. With a higher Ni content and therefore stacking fault energy, the maximum in twin boundary fraction is increasing and is shifted towards greater sliding speeds. The evolution of the grain boundary fraction follows the same trend as for the twin boundaries with the difference that their formation is happening at slightly higher sliding speeds. Note however, that the changes in the twin boundary and grain boundary fractions may already be (partially) obsolete, as shear dominates the system behavior at the point where twin and grain boundaries increase dramatically. Panel (c) shows the shear strain rate on a logarithmic scale, once for the near-surface region (the 2 nm directly below the surface; dashed lines) and once for the "bulk" (the 32 nm below the surface layer; solid lines). A dotted green curve represents ideal Couette flow, i.e., the shear behavior that would be expected of a viscous fluid. At the lowest sliding velocities, the mean shear strain rates near the surface and in the bulk differ by roughly 2.5 orders of magnitude. Note that a value of 10^6 constitutes the approximate detection limit, which is determined by the size of the system, the occurring speeds, as well as the numerical accuracy. It seems as if the onset of shear layer formation was relatively independent of the alloy composition. Around 80 m/s, the mean shear strain rate in the bulk rises to just below 10^9 1/s for the first time in all four systems, while the respective value in the near-surface layer is still rising at the same rate as for lower speeds. In the sliding speed range between 160 and 640 m/s, depending on the composition, the bulk and near-surface values of the shear strain rate approach to within half an order of magnitude, with the near-surface curves exhibiting a noticeable dip. At these sliding speeds the shear layer becomes less and less localized and the entire bulk is shearing, resulting in a higher resistance to shearing in the near-surface regions, which explains the dip in shear strain rate. Note how close the solid "bulk" curves come to ideal Couette behavior in this velocity range. The locations of the maxima for the bulk shear strain rates of neighboring alloy compositions lie approximately one power of 2 apart and almost coincide with those for ΔGB. This overlap of the maxima is not surprising as more defects can be expected if plastic deformation is progressing further into the material.

The relative real contact area (panel d) remains below 30% up to 40 m/s, but then starts growing up to 70% as maximum contact conformity is approached due to plastic deformation of the substrate material, which then flows into the asperities of the undeformed counterbody. At speeds greater than where the maximum contact area is reached, the latter takes a steep decline, dropping below 40% or even down to 10% at the highest considered sliding speeds. This decline is accompanied by a noticeable increase in the mean contact temperature, reaching or even surpassing the bulk melting temperature of that alloy, as the sliding speed becomes so high that the thermostat does not have sufficient time to remove the frictional heat from the system, see panel (e). Here it has to be considered that maximum temperatures are even higher since these temperatures are averaged over elements encompassing around 1 400 atoms. Note that the mean contact temperature cannot be separated from the non-contact counterpart up to sliding speeds of around 320–640 m/s, which is where the temperature distribution shifts from a unimodal to a bimodal shape, see the time-resolved temperature distribution maps for CuNi60 Fig. S3 (Supplementary Information). With the emergence of the second, much broader peak at higher temperatures that represents the contact temperature, and the re-emergence of a sharp low-temperature peak near 300 K representing the non-contact surface regions, it is now possible to cleanly differentiate between the two (compare the lower two panels in Fig. S3). The fraction of surface elements contributing to the contact temperature is only slightly larger than the corresponding relative real contact area to the right of the respective maximum values.

The shear stress σ_x shown in panel (f) provides the quantification of the resistance of the surfaces to sliding, and is hence the closest embodiment of friction. It increases with sliding velocity, reaching a composition dependent peak and then dropping again at higher sliding velocities. This is in good agreement with the development of the real contact area, which first increases with higher sliding velocities as the contact gets more conformal due to softening of the material and more pronounced plastic deformation takes place, see panel (d). The increase in the maximum value of σ_x for compositions with higher Ni concentration correlates well with the trend of the twin boundary and stacking fault fraction in panel (a). Pure Ni shows the highest σ_x over sliding velocity due to its highest stacking fault energy and higher hardness compared to the other alloys in the graph, leading to additional shear stress needed to overcome the resistance of the system to deform permanently. As for ΔTB, we also observe that the maximum in σ_x is shifted to higher sliding velocities for alloys containing more Ni. At the same time, Ni-richer alloys feature smaller contact temperatures at corresponding sliding velocities, see panel (e). Therefore, softening of material at the surface and possible phase transitions from solid to liquid with a subsequent drop in shear stress occur at higher sliding velocities (recall Fig. 3), resulting in a composition dependent critical sliding velocity after which resistance to shear starts decreasing again.

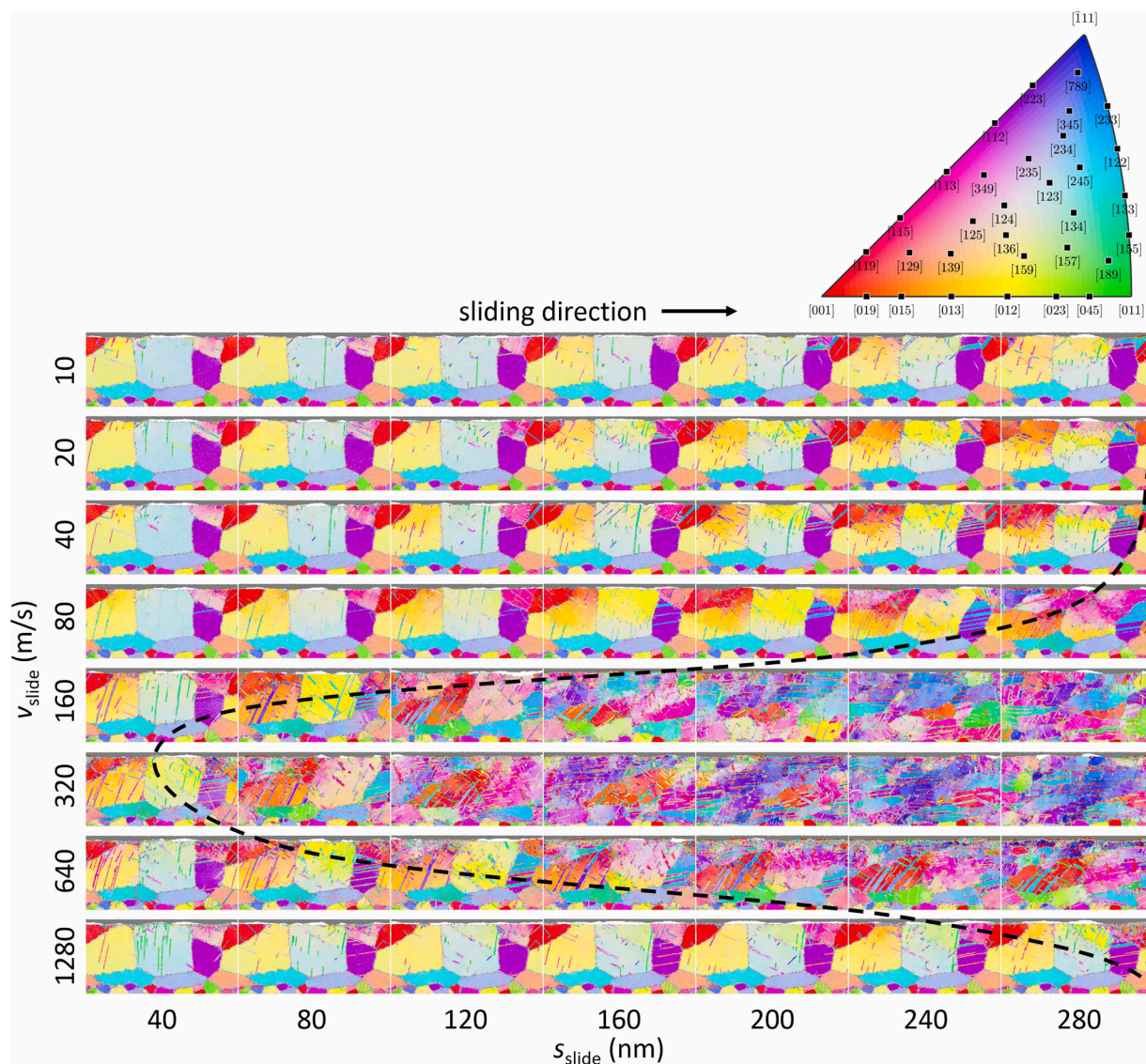Several works in the existing literature spanning six decades have

Fig. 2. Time-resolved comparison of representative tomographs of CuNi25 at 0.7 GPa at various sliding velocities, colored by grain orientation according to EBSD-IPF standard (see legend annotated with several low-index directions). Other compositions exhibit very similar behavior. Vertical axis: variation of sliding velocity. Horizontal axis: increasing sliding distance. The dashed line loosely separates the regions of low and high microstructural impact.

found evidence of a decrease in friction at very high velocities, which we compare with our results for CuNi5 in Fig. S6 in the Supplementary Material. The most striking resemblance of the data is the narrow velocity range above which the friction drops. Seminal research work by Bowden and Freitag [28] already indicated that copper tends to behave as a molten liquid with a high viscosity at the surface when subjected to high sliding velocities. Furthermore, Lin et al. [45] presented results very similar to those in our study. They studied Cu/Fe and Ag/Cu tribopairs using MD and focused on microstructural changes and interface friction in a sliding velocity range from 25 to 1000 m/s. Interestingly, the plot of friction force per area over sliding velocity clearly displays a rise in friction force with increasing sliding velocity with a peak around 300 m/s for Cu/Fe tribopairs. After having reached the peak, the friction force decreases again due to frictional heating and local softening/melting, which is known as velocity weakening [28,44]. In our work, we can provide an extensive materials scientific explanation for this behavior.

We now reduce all of the findings above to a single graph in an attempt to identify the links between all of the occurring mechanisms and phenomena in a master plot, see Fig. 6. To do so, it was necessary to define non-dimensional quantities with their most relevant ranges between zero and one. We thus define a quantity we call "microstructural integrity" as $1 - \langle \Delta GB \rangle - \langle \Delta TB \rangle$, which is 1 for a polycrystalline sample that does not undergo any plastic deformation and smaller for samples that have more twins, grain boundaries, or other defects. The normalized real contact area $A_{contact}/A_0$ already fulfills our requirement of being non-dimensionalized and between zero and one. We normalize the contact temperature by the melting temperature, $T_{contact}/T_m$, and the sliding velocity by the speed of sound in the respective alloy, v_{slide}/c_s. Finally, we normalize the bulk shear strain rate by the value associated with ideal Couette flow, which we name $(dv_x/dz)_{norm}$. The result of plotting the measured non-dimensionalized quantities over the normalized sliding speed is shown in Fig. 6. In the Supplementary Material, we present an arguably busy "precursor" plot (Fig. S5), which serves to prove that none of the data obtained from our simulations was left out in producing the cleaned-up version shown here. To make Fig. 6, the bundles of curves were replaced by their envelopes and a hand-fitted median curve that resembles the general trend.

Let us now discuss the plot in Fig. 6 from left to right, i.e., with increasing sliding speed. The yellow arrow in the bottom left corner of
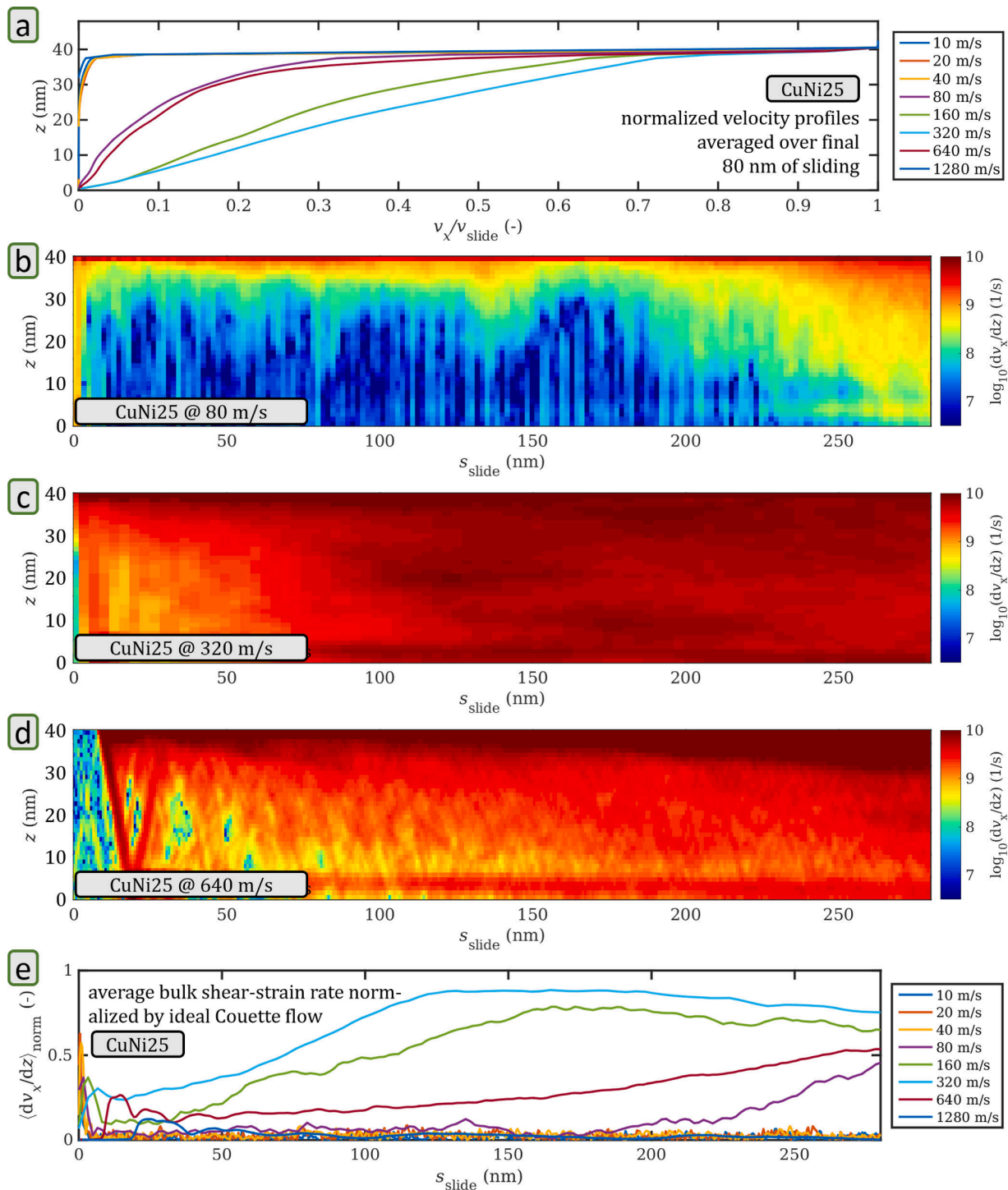
Fig. 3. About the shear strain rate. (a) Velocity profiles, averaged over the final 80 nm of sliding and normalized by sliding speed for all CuNi25 systems. (b–d) Three representative logarithmic heat maps of the shear strain rate for CuNi25 at 80 m/s (onset of strong influence of sliding speed on plastic deformation) 320 m/s (maximum influence of sliding speed), and 640 m/s (decreasing influence of sliding speed). Note that temperature (not systematically varied here, but studied in previous work [33,55]) also has an influence on the appearance of such maps. (e) Depth-averaged bulk shear strain rate (excluding 2 nm surface layer), normalized by ideal Couette flow, as a function of sliding distance for all CuNi25 systems.

the figure labeled "Ashby world" attempts to put this plot into perspective with respect to the seminal deformation mechanism maps published by Frost and Ashby in the 1970s and 1980s [63,64]. These maps give an extremely detailed account of how a plethora of materials with grain sizes in the micrometer range react to shear stresses 1–6 orders of magnitude below those discussed here, while the shear strain rates encountered there lie some 6–10 orders of magnitude below ours.

At the lower end of the speed range shown in Fig. 6, the microstructural integrity is almost one, the typical normalized contact area is around 25%, the bulk shear strain rate is zero, and, the contact temperature is equal to the thermostat target temperature of $T_{contact}/T_m = 0.2$. This first regime, where the shear strain rate is independent of the sliding speed, we call "classical plasticity" (Ia). As sv_{slide}/c_s exceeds 1%, we see the microstructural integrity slowly decline as plastic deformation sets in,
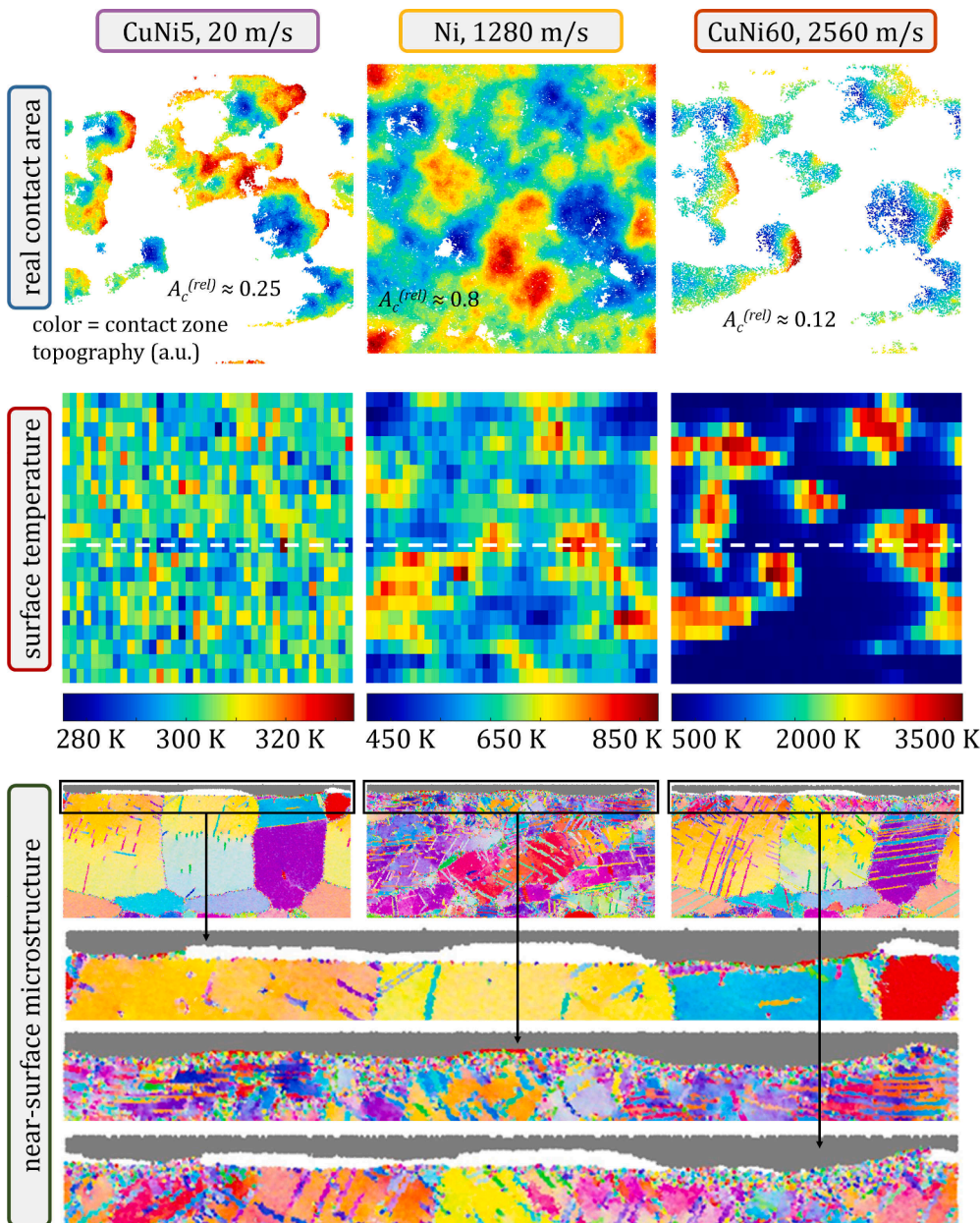
Fig. 4. Snapshots of $A_c^{(rel)}$ (top row), the surface temperature T_{surf} (center row), and the (near-surface) microstructure at the position marked by the dashed white line (bottom row) after sliding 280 nm for three representative systems. The color coding for $A_c^{(rel)}$ is by z value of the contact atoms and therefore gives a feeling for the contact zone topography. The systems were carefully selected to exemplify moderate values of $A_c^{(rel)}$ at low sliding velocities paired with low surface temperatures (left); maximum contact conformity paired with elevated surface temperatures (center); and the strongly reduced contact area at very high sliding velocity, paired with temperature peaks beyond the melting point in the remaining contact spots, with relatively low temperatures in the non-contact regions (right). While it would have been possible to select three different sliding velocities of a single alloy that would have behaved similarly, the shown examples best illustrate the considerable differences between the velocity regimes and are most suitable for discussion in the main text.

reflected by a significant increase in twin and grain boundary formation (see Fig. 2), which leads to a more conformal interface with a higher contact area. This in turn allows the deformation to propagate deeper into the bulk, thus raising the shear strain rate, while the contact temperature still remains constant. The increase in shear strain rate subsequently leads to stronger plastic deformation, providing positive feedback and accelerating the above process. We consider this region up to 5% of the speed of sound a transition to fluid-like behavior (Ib). This trend continues until the contact area and the bulk shear strain rate reach their maxima at approximately $v_{slide}/c_s = 10$ and 15%, respectively, the latter coinciding with the minimum of the microstructural integrity. This regime is characterized by a fluid-like bulk-response with the shear strain rate being close to ideal Couette flow and is denoted as such (II) in Fig. 6. In this sliding speed range, the contact temperature starts to rise very slowly, until it exhibits a sharp increase around $v_{slide}/c_s = 25\%$, at which point both the contact area and the shear strain rate have dropped again below 50% and also the microstructural integrity has started its recovery. This upper regime is characterized by the (re-)localization of the shear interface (III). As the normalized sliding speed

exceeds 60%, the contact temperature has risen beyond the melting temperature of the respective alloys. At this point, the bulk shear strain rate has dropped to zero, the contact area has returned to the value it assumed at low sliding speeds or even below, while also the microstructural integrity has greatly recovered with some residual plastic deformation. Until the maxima in contact area and shear strain rate are reached the resistance to shear (and hence friction) is simultaneously increasing as more energy has to be dissipated to plastically deform the material. The combined action of an increase in temperature inducing thermal softening and eventually melting of the surface-near material, (re-)localization of the shear interface, and a decrease in real contact lead to a decrease in resistance to shear and ultimately friction for higher sliding speeds.

The results and analyses presented in this paper are far-reaching and can be easily transposed into other contexts, providing guidance for the discovery of important mechanisms that control interfacial behavior across a range of materials and applications. There exist many analogies between the behavior of the polycrystalline systems studied here and the response of other confined systems subjected to shear in which phase
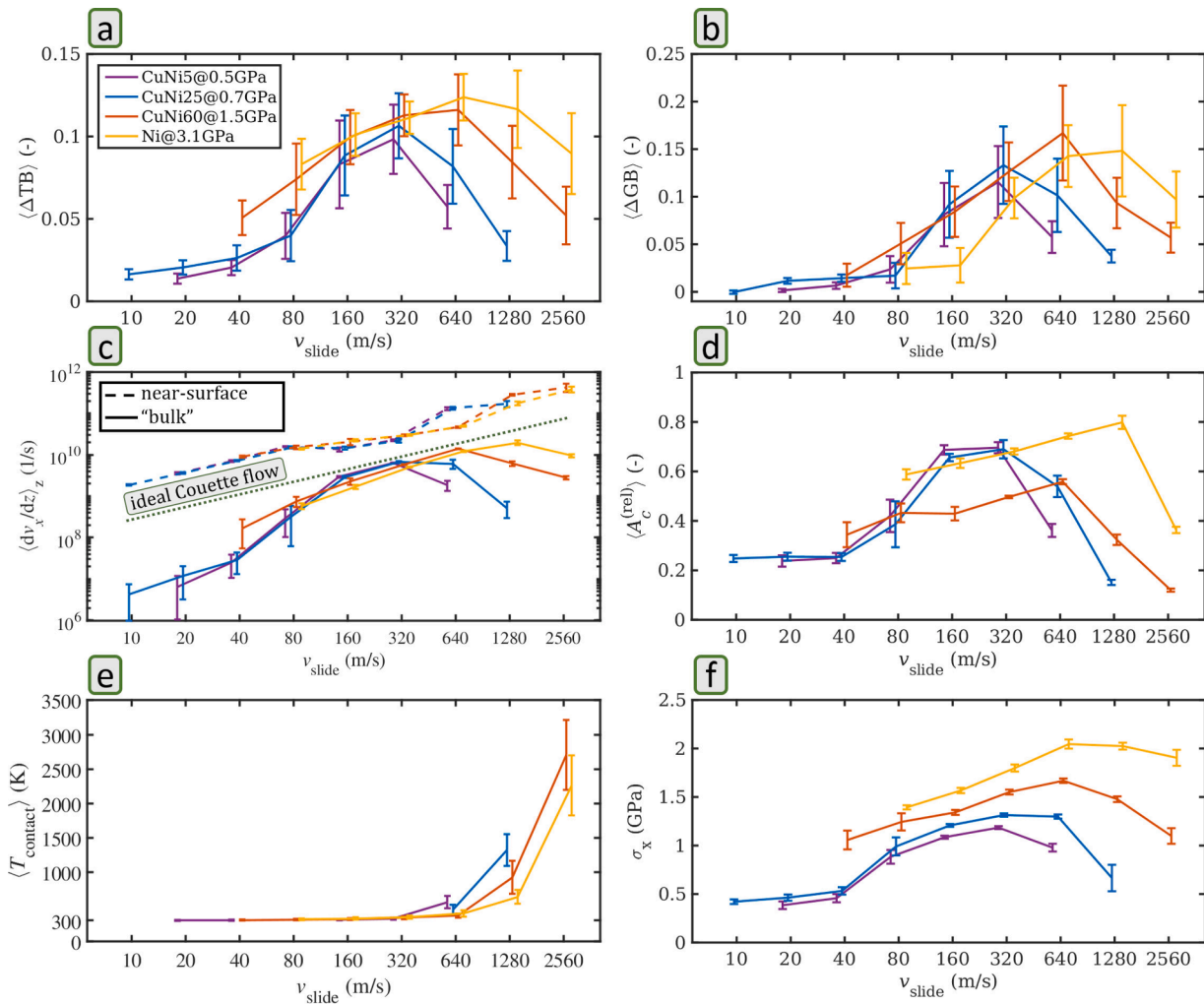
Fig. 5. Mean equilibrium values of the increase in the twin boundary and stacking fault fraction ΔTB (a), the grain boundary and defect fraction ΔGB (b), the depth-averaged shear strain rate in the near-surface region and the bulk of the sample (logarithmic scale, c) and the relative real contact area (d), as well as the average contact temperature (e) and shear stress (f) as a function of sliding velocity. The normal loads for the respective alloys were chosen so that they have similar dominant deformation mechanisms at 80 m/s (cf. Fig. 1).
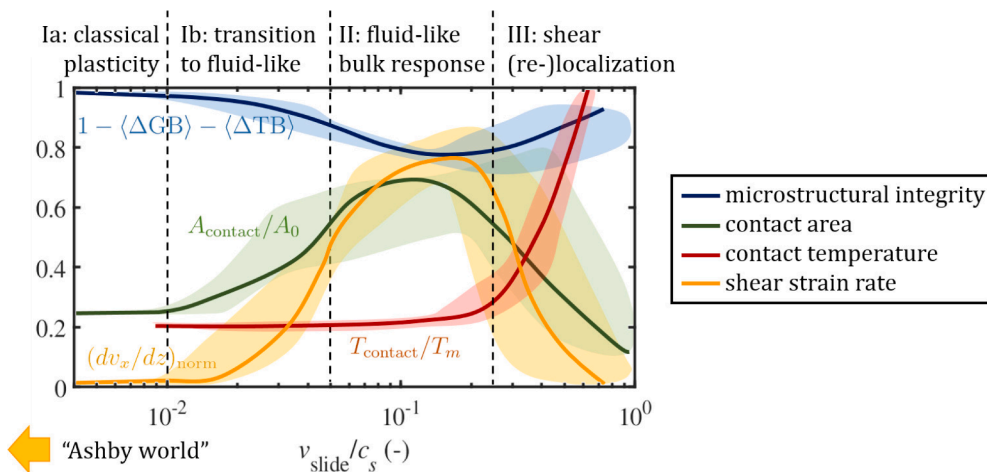

Fig. 6. Master plot of the non-dimensional quantities of microstructural integrity $1 - \langle \Delta \text{GB} \rangle - \langle \Delta \text{TB} \rangle$, normalized real contact area A_{contact}/A_0, homologous contact temperature T_{contact}/T_m, and bulk shear strain rate normalized by ideal Couette flow, $(dv_x/dz)_{\text{norm}}$, as a function of the sliding speed normalized by the speed of sound, v_{slide}/c_s, with hand-fitted annotated trend curves and data variance ranges. A version of this figure with alloy-resolved curves extracted from the data in Fig. 5 is available in the Supplementary Material as Fig. S5.

transitions govern the behavior of interfaces and often also the tribological response. Yet, often little is known about the physical process underlying the material transformations and changes in structure of the resulting phases. It is particularly interesting to note that the transitions

from solid-like to liquid-like behavior reported here is also seen in brittle covalent crystals (such as silicon and diamond), where for example shear-driven amorphization is promoted by the formation of a liquid-like phase due to localized melting, which causes Couette-type flow at

the sliding interfaces [65].

A number of similarities can also be found with respect to confined fluids, whose behavior under combined compressive and shear stress is of high relevance in technology, and which often undergo the opposite transition upon application of large normal loads [66–69]. In such scenarios, viscoplastic behavior of the "liquid" system can be experienced under shear, and dislocation-like structures emerge. Furthermore wall-slip, analogous to that seen in region (III) of the map in Fig. 6, also appears at the solid-solid and solid-liquid interfaces developing in such systems. It is worth mentioning that the mechanisms unraveled while studying our systems across a range of sliding velocities, loads, and temperatures [33,39] can also shed light on the formation of shear bands in bulk metallic glasses (see, e.g., Ref. [70]), where the temperature rises due to friction forces in the viscous, supercooled, liquid thin layer in the shear bands, as well as on the formation of white etching cracks [71,72]. A further aspect to be considered is the future development of a methodology that captures the evolution of the surface and links the surface melting to the surface evolution, therefore adding to the recent evidence provided for the emergence of small-scale surface roughness due to deformation [73].

Our transition velocities marking the onset of melting are in astonishing agreement with recent experimental studies of microparticles impacting on a range of metallic surfaces at ballistic velocities [27,74, 75]. They find that the ratio of particle rebound velocity to impact velocity scales with speed according to a power law up to impact velocities of 400–600 m/s, but then it starts deviating considerably. This deviation marks the transition to a different physical regime, and it can be quantified as an excess energy that is available for other mechanisms to occur, in particular local melting of the substrate due to adiabatic heating [27]. A comparison of the small melted volumes with their large lateral extent suggests very thin melted and resolidified layers of substrate material, which compares excellently with our own findings.

4. Conclusion and outlook

This study has provided a systematic assessment of the effect of sliding speed on microstructural evolution and deformation mechanisms using large-scale molecular dynamics simulations. Our analyses show the emergence of a clear trend that links dislocation activity as well as twin and grain boundary formation via the evolution of contact area and temperature gradients to the sliding speed and shear strain rate, demonstrating the intimate link between the microstructural evolution of the system and the resistance to shear.

The transitions between different deformation and shear resistance regimes can be identified in the final master plot, which clearly indicates three deformation mechanism regimes. In the first, where sliding speeds are below 1% of the speed of sound, plasticity remains virtually velocity-independent (I). After a transition region, the bulk behaves predominantly fluid-like at sliding speeds ranging from 5–25% of the speed of sound (II). At even higher sliding speeds, the shear (re-)localizes at the surface, facilitated mainly by local melting below the asperities, which leads to the formation of lubrication patches, a reduction in real contact area and shear stress, as well as a widely unperturbed microstructure throughout most of the polycrystalline alloy (III).

The implications of our findings are broad, as this study demonstrates that at the surface and near-surface, deformation mechanisms are strongly affected by the sliding speed. For example, an increase in twin and grain boundaries or localized melting, significantly triggered by an increase in velocity, affect the resistance of the material to shear. Our results, which also mechanistically explain the response obtained experimentally from impacting on a range of metallic surfaces at ballistic velocities, can be directly applied to high-speed manufacturing, forming processes, automotive crashworthiness, and design of impact resistance materials.

Regarding the design of materials, this study also provides a guideline for the most promising parameters that may be tuned to improve the performance of materials in terms of resistance to shear at high sliding speeds: changes induced to improve the resistance to plastic deformation by changing an alloy's composition (e.g., increasing the stacking fault energy and introducing precipitates to interlock dislocations and hinder the formation of twins) can be coupled with the manipulation of the thermal properties (e.g., melting point) in order to delay/accelerate shear localization.

Data availability

The raw/processed data required to reproduce these findings cannot be shared at this time as the data also forms part of an ongoing study.

CRediT authorship contribution statement

S.J. Eder: Conceptualization, Methodology, Software, Formal analysis, Data curation, Visualization, Writing – original draft. **P.G. Grützmacher:** Investigation, Writing – original draft. **M. Rodríguez Ripoll:** Investigation, Writing – original draft. **C. Gachot:** Conceptualization, Investigation, Resources, Supervision, Writing – original draft. **D. Dini:** Conceptualization, Investigation, Supervision, Writing – original draft.

Declaration of Competing Interest

The authors declare that they have no known competing financial interests or personal relationships that could have appeared to influence the work reported in this paper.

Acknowledgments

Supplementary material

Supplementary material associated with this article can be found, in the online version, at 10.1016/j.apmt.2022.101588

References

[1] M. Ye, H. Gong, R. Xiong, H. Mu, Research on the battery charging strategy with charging and temperature rising control awareness, IEEE Access 6 (2018) 64193–64201.

[2] W.L. Johnson, Bulk amorphous metal-an emerging engineering material, JOM 54 (3) (2002) 40–43.

[3] T. Voisin, M.D. Grapes, T.T. Li, M.K. Santala, Y. Zhang, J.P. Ligda, N.J. Lorenzo, B. E. Schuster, G.H. Campbell, T.P. Weihs, In situ TEM observations of high-strain-rate deformation and fracture in pure copper, Mater. Today 33 (2020) 10–16.

[4] N.T.-C. Nguyen, P. Asghari-Rad, P. Sathiyamoorthi, A. Zargaran, C.S. Lee, H.S. Kim, Ultrahigh high-strain-rate superplasticity in a nanostructured high-entropy alloy, Nat. Commun. 11 (1) (2020) 1–7.

[5] A.I. Vakis, V.A. Yastrebov, J. Scheibert, L. Nicola, D. Dini, C. Minfray, A. Almqvist, M. Paggi, S. Lee, G. Limbert, et al., Modeling and simulation in tribology across scales: an overview, Tribol. Int. 125 (2018) 169–199.

[6] C.A. Coulomb, Théorie des Machines Simples en Ayant Égard au Frottement de Leurs Parties et à la Roideur des Cordages, Bachelier, 1821.

[7] M.A. Chowdhury, M.K. Khalil, D.M. Nuruzzaman, M.L. Rahaman, The effect of sliding speed and normal load on friction and wear property of aluminum, Int. J. Mech. Mechatron.Eng. 11 (1) (2011) 45–49.

[8] A. Molinari, Y. Estrin, S. Mercier, Dependence of the coefficient of friction on the sliding conditions in the high velocity range, J. Tribol. 121 (1999) 35–41.

[9] S.C. Lim, M.F. Ashby, J.H. Brunton, The effects of sliding conditions on the dry friction of metals, Acta Metall. 37 (3) (1989) 767–772.

[10] S.C. Lim, M.F. Ashby, Overview no. 55 wear-mechanism maps, Acta Metall. 35 (1) (1987) 1–24.

[11] P.J. Blau, Friction Science and Technology: From Concepts to Applications, CRC press, 2008.

[12] C.B. Finfrock, M.M. Thrun, D. Bhattacharya, T.J. Ballard, A.J. Clarke, K.D. Clarke, Strain rate dependent ductility and strain hardening in Q&P steels, Metall. Mater. Trans. A 52 (3) (2021) 928–942.

[13] S.J. Eder, P.G. Grützmacher, T. Spenger, H. Heckes, H. Rojacz, A. Nevosad, F. Haas, Experimentally validated atomistic simulation of the effect of relevant grinding parameters on work piece topography, internal stresses, and microstructure, Friction 10 (4) (2022) 608–629.

[14] P. Stoyanov, K.M. Harrington, A. Frye, Insights into the tribological characteristic of cu-based coatings under extreme contact conditions, JOM (2020) 1–7.

[15] Y. Yang, Z. Xinming, L. Zhenghua, L. Qingyun, Adiabatic shear band on the titanium side in the Ti/mild steel explosive cladding interface, Acta Mater. 44 (2) (1996) 561–565.

[16] R.S. Montgomery, Friction and wear at high sliding speeds, Wear 36 (3) (1976) 275–298.

[17] D. Gerada, A. Mebarki, N.L. Brown, C. Gerada, A. Cavagnino, A. Boglietti, High-speed electrical machines: technologies, trends, and developments, IEEE Trans. Ind. Electron. 61 (6) (2013) 2946–2959.

[18] B. Gurrutxaga-Lerma, J. Verschueren, A.P. Sutton, D. Dini, The mechanics and physics of high-speed dislocations: a critical review, Int. Mater. Rev. 66 (4) (2021) 215–255.

[19] H. Fan, Q. Wang, J.A. El-Awady, D. Raabe, M. Zaiser, Strain rate dependency of dislocation plasticity, Nat. Commun. 12 (1) (2021) 1–11.

[20] F.C. Salvado, F. Teixeira-Dias, S.M. Walley, L.J. Lea, J.a.B. Cardoso, A review on the strain rate dependency of the dynamic viscoplastic response of fcc metals, Prog. Mater. Sci. 88 (2017) 186–231.

[21] P. Grützmacher, C. Gachot, S.J. Eder, Visualization of microstructural mechanisms in nanocrystalline ferrite during grinding, Mater. Des. 195 (2020) 109053.

[22] S.J. Eder, S. Leroch, P.G. Grützmacher, T. Spenger, H. Heckes, A multiscale simulation approach to grinding ferrous surfaces for process optimization, Int. J. Mech. Sci. 194 (2021) 106186.

[23] C.D.P. Rodrigues, Design of a high-speed transmission for an electric vehicle, 2018.

[24] M. Khaire, Role of bearings in new generation automotive vehicles: powertrain. Advanced Applications of Hydrogen and Engineering Systems in the Automotive Industry, IntechOpen, 2020.

[25] T. Noguchi, Y. Takata, Y. Yamashita, Y. Komatsu, S. Ibaraki, 220,000-r/min, 2-kW permanent magnet motor drive for turbocharger. International Power Electronics Conference (IPEC-Niigata 2005), 2005, p. 52.

[26] I.A. Bataev, D.V. Lazurenko, S. Tanaka, K. Hokamoto, A.A. Bataev, Y. Guo, A. M. Jorge Jr., High cooling rates and metastable phases at the interfaces of explosively welded materials, Acta Mater. 135 (2017) 277–289.

[27] J. Lienhard, D. Veysset, K.A. Nelson, C.A. Schuh, Melting and ejecta produced by high velocity microparticle impacts of steel on tin, J. Appl. Mech. 88 (11) (2021).

[28] F.P. Bowden, E.H. Freitag, The friction of solids at very high speeds: I. Metal on metal; II. Metal on diamond. Proceedings of the Royal Society of London. Series A. Mathematical and Physical Sciences vol. 248, 1958, pp. 350–367.

[29] M. Varga, S. Leroch, S.J. Eder, H. Rojacz, M. Rodríguez ripoll, Influence of velocity on high-temperature fundamental abrasive contact: a numerical and experimental approach, Wear 426 (2019) 370–377.

[30] E. Gnecco, R. Bennewitz, T. Gyalog, C. Loppacher, M. Bammerlin, E. Meyer, H.-J. Güntherodt, Velocity dependence of atomic friction, Phys. Rev. Lett. 84 (6) (2000) 1172.

[31] P.A. Romero, T.T. Järvi, N. Beckmann, M. Mrovec, M. Moseler, Coarse graining and localized plasticity between sliding nanocrystalline metals, Phys. Rev. Lett. 113 (3) (2014) 036101.

[32] P.G. Grützmacher, S. Rammacher, D. Rathmann, C. Motz, F. Mücklich, S. Suarez, Interplay between microstructural evolution and tribo-chemistry during dry sliding of metals, Friction 7 (6) (2019) 637–650.

[33] S.J. Eder, P.G. Grützmacher, M.R. Ripoll, D. Dini, C. Gachot, Effect of temperature on the deformation behavior of copper nickel alloys under sliding, Materials 14 (1) (2021) 60.

[34] K. Holmberg, A. Matthews, Coatings Tribology: Properties, Mechanisms, Techniques and Applications in Surface Engineering, Elsevier, 2009.

[35] F. Findik, Latest progress on tribological properties of industrial materials, Mater. Des. 57 (2014) 218–244.

[36] N. Argibay, M. Chandross, S. Cheng, J.R. Michael, Linking microstructural evolution and macro-scale friction behavior in metals, J. Mater. Sci. 52 (5) (2017) 2780–2799.

[37] T.D.B. Jacobs, C. Greiner, K.J. Wahl, R.W. Carpick, Insights into tribology from in situ nanoscale experiments, MRS Bull. 44 (6) (2019) 478–486.

[38] S. Okita, E. Miyoshi, S. Sakane, T. Takaki, M. Ohno, Y. Shibuta, Grain growth kinetics in submicrometer-scale molecular dynamics simulation, Acta Mater. 153 (2018) 108–116.

[39] S.J. Eder, M.R. Ripoll, U. Cihak-Bayr, D. Dini, C. Gachot, Unraveling and mapping the mechanisms for near-surface microstructure evolution in CuNi alloys under sliding, ACS Appl. Mater. Interfaces 12 (28) (2020) 32197–32208.

[40] A. Dollmann, A. Kauffmann, M. Heilmaier, A.S. Tirunilai, L.S. Mantha, C. Kübel, S. J. Eder, J. Schneider, C. Greiner, Dislocation-mediated and twinning-induced plasticity of cocrfemnni in varying tribological loading scenarios, 2021, ArXiv preprint, cond-mat.mtrl-sci:2111.06652.

[41] J. Verschueren, B. Gurrutxaga-Lerma, D.S. Balint, A.P. Sutton, D. Dini, Instabilities of high speed dislocations, Phys. Rev. Lett. 121 (14) (2018) 145502.

[42] C.A. Powell, H.T. Michels, Copper-nickel alloys for seawater corrosion resistance and anti-fouling: a state of the art review. CORROSION 2000, NACE International, 2000.

[43] M. Noguchi, Sliding member, rotary device, and method for manufacturing sliding member, 2019, US Patent 10,505,328.

[44] J.E. Hammerberg, B.L. Holian, J. Röder, A.R. Bishop, S.J. Zhou, Nonlinear dynamics and the problem of slip at material interfaces, Phys. D 123 (1–4) (1998) 330–340.Annual International Conference of the Center for Nonlinear Studies.

[45] E.-Q. Lin, L.-S. Niu, H.-J. Shi, Z. Duan, Molecular dynamics simulation of nano-scale interfacial friction characteristic for different tribopair systems, Appl. Surf. Sci. 258 (6) (2012) 2022–2028.

[46] S.J. Plimpton, Fast parallel algorithms for short-range molecular dynamics, J. Comput. Phys. 117 (1995) 1–19.

[47] S.J. Eder, D. Bianchi, U. Cihak-Bayr, K. Gkagkas, Methods for atomistic abrasion simulations of laterally periodic polycrystalline substrates with fractal surfaces, Comput. Phys. Commun. 212 (2017) 100–112.

[48] S.J. Eder, U. Cihak-Bayr, C. Gachot, M.R. Ripoll, Interfacial microstructure evolution due to strain path changes in sliding contacts, ACS Appl. Mater. Interfaces 10 (28) (2018) 24288–24301.

[49] G. Bonny, R.C. Pasianot, N. Castin, L. Malerba, Ternary Fe–Cu–Ni many-body potential to model reactor pressure vessel steels: first validation by simulated thermal annealing, Philos. Mag. 89 (34–36) (2009) 3531–3546.

[50] C. Frank, Orientation mapping: 1987 mrs fall meeting von Hippel award lecture, MRS Bull. 13 (3) (1988) 24–31.

[51] J.P. Ewen, S.E. Restrepo, N. Morgan, D. Dini, Nonequilibrium molecular dynamics simulations of stearic acid adsorbed on iron surfaces with nanoscale roughness, Tribol. Int. 107 (2017) 264–273.

[52] S.J. Eder, U. Cihak-Bayr, A. Vernes, G. Betz, Evolution of topography and material removal during nanoscale grinding, J. Phys. D 48 (2015) 465308.

[53] W. Li, S. Lu, Q.-M. Hu, S.K. Kwon, B. Johansson, L. Vitos, Generalized stacking fault energies of alloys, J. Phys.Cond.Mat. 26 (26) (2014) 265005.

[54] S.J. Eder, U. Cihak-Bayr, D. Bianchi, G. Feldbauer, G. Betz, Thermostat influence on the structural development and material removal during abrasion of nanocrystalline ferrite, ACS Appl. Mater. Interfaces 9 (15) (2017) 13713–13725.

[55] S.J. Eder, P.G. Grützmacher, M.R. Ripoll, J.F. Belak, Elucidating the onset of plasticity in sliding contacts using differential computational orientation tomography, Tribol. Lett. 69 (3) (2021) 1–15.

[56] P.M. Larsen, S. Schmidt, S. Jakob, Robust structural identification via polyhedral template matching, Modell. Simul. Mater. Sci. Eng. 24 (5) (2016) 055007.

[57] A. Stukowski, Visualization and analysis of atomistic simulation data with OVITO–the open visualization tool, Modell. Simul. Mater. Sci. Eng. 18 (1) (2009) 015012.

[58] F. Bachmann, R. Hielscher, H. Schaeben, Texture analysis with MTEX–free and open source software toolbox. Solid State Phenomena vol. 160, Trans Tech Publ, 2010, pp. 63–68.

[59] G. Nolze, R. Hielscher, Orientations–perfectly colored, J. Appl. Crystallogr. 49 (5) (2016) 1786–1802.

[60] H. Tsuzuki, P.S. Branicio, J.P. rino, Structural characterization of deformed crystals by analysis of common atomic neighborhood, Comput. Phys. Commun. 177 (6) (2007) 518–523.

[61] S.J. Eder, U. Cihak-Bayr, D. Bianchi, Large-scale molecular dynamics simulations of nanomachining, **In: Advanced Machining Processes:** Innovative Modeling Techniques, CRC Press (2017) 141.

[62] S. Eder, A. Vernes, G. Betz, Methods and numerical aspects of nanoscopic contact area estimation in atomistic tribological simulations, Comput. Phys. Commun. 185 (2014) 217–228.

[63] H.J. Frost, M.F. Ashby, A Second Report on Deformation Mechanism Maps. Technical Report, Harvard University (Cambridge, MA), Division of Engineering and Applied Physics, 1973.

[64] H.J. Frost, M.F. Ashby, Deformation Mechanism Maps: The Plasticity and Creep of Metals and Ceramics, Pergamon Press, 1982.

[65] G. Moras, A. Klemenz, T. Reichenbach, A. Gola, H. Uetsuka, M. Moseler, L. Pastewka, Shear melting of silicon and diamond and the disappearance of the polyamorphic transition under shear, Phys. Rev. Mater. 2 (8) (2018) 083601.

[66] D.M. Heyes, E.R. Smith, D. Dini, H.A. Spikes, T.A. Zaki, Pressure dependence of confined liquid behavior subjected to boundary-driven shear, J. Chem. Phys. 136 (13) (2012) 134705.

[67] C. Gattinoni, D.M. Heyes, C.D. Lorenz, D. Dini, Traction and nonequilibrium phase behavior of confined sheared liquids at high pressure, Phys. Rev. E 88 (5) (2013) 052406.

[68] S. Maćkowiak, D.M. Heyes, D. Dini, A.C. Brańka, Non-equilibrium phase behavior and friction of confined molecular films under shear: a non-equilibrium molecular dynamics study, J. Chem. Phys. 145 (16) (2016) 164704.

[69] J.P. Ewen, C. Gattinoni, J. Zhang, D.M. Heyes, H.A. Spikes, D. Dini, On the effect of confined fluid molecular structure on nonequilibrium phase behaviour and friction, Phys. Chem. Chem. Phys. 19 (27) (2017) 17883–17894.

[70] S.V. Ketov, D.V. Louzguine-Luzgin, Localized shear deformation and softening of bulk metallic glass: stress or temperature driven? Sci. Rep. 3 (1) (2013) 1–6.

[71] W. Solano-Alvarez, H. Bhadeshia, White-etching matter in bearing steel. Part II: distinguishing cause and effect in bearing steel failure, Metall. Mater. Trans. A 45 (11) (2014) 4916–4931.

[72] F. Manieri, K. Stadler, G.E. Morales-Espejel, A. Kadiric, The origins of white etching cracks and their significance to rolling bearing failures, Int. J. Fatigue 120 (2019) 107–133.

[73] A.R. Hinkle, W.G. Nöhring, R. Leute, T. Junge, L. Pastewka, The emergence of small-scale self-affine surface roughness from deformation, Sci. Adv. 6 (7) (2020) Eaax0847.

[74] M. Hassani-Gangaraj, D. Veysset, K.A. Nelson, C.A. Schuh, In-situ observations of single micro-particle impact bonding, Scr. Mater. 145 (2018) 9–13.

[75] Y. Sun, D. Veysset, K.A. Nelson, C.A. Schuh, The transition from rebound to bonding in high-velocity metallic microparticle impacts: jetting-associated power-law divergence, J. Appl. Mech. 87 (9) (2020) 091002.